Optical valley Hall effect for highly valley-coherent exciton-polaritons in an atomically thin semiconductor

Nils Lundt¹, Łukasz Dusanowski¹, Evgeny Sedov^{2,3}, Petr Stepanov⁴, Mikhail M. Glazov⁵, Sebastian Klembt¹, Martin Klaas¹, Johannes Beierlein¹, Ying Qin⁶, Sefaattin Tongay⁶, Maxime Richard³, Alexey V. Kavokin^{7,8,9}, Sven Höfling^{1,10} and Christian Schneider^{1*}

Spin-orbit coupling is a fundamental mechanism that connects the spin of a charge carrier with its momentum. In the optical domain, an analogous synthetic spin-orbit coupling is accessible by engineering optical anisotropies in photonic materials. Both yield the possibility of creating devices that directly harness spin and polarization as information carriers. Atomically thin transition metal dichalcogenides promise intrinsic spin-valley Hall features for free carriers, excitons and photons. Here we demonstrate spin- and valley-selective propagation of exciton-polaritons in a monolayer of MoSe₂ that is strongly coupled to a microcavity photon mode. In a wire-like device we trace the flow and helicity of exciton-polaritons expanding along its channel. By exciting a coherent superposition of K and K' tagged polaritons, we observe valley-selective expansion of the polariton cloud without either an external magnetic field or coherent Rayleigh scattering. The observed optical valley Hall effect occurs on a macroscopic scale, offering the potential for applications in spin-valley-locked photonic devices.

pin-valley locking is a striking feature of free charge carriers and excitons that emerges in monolayers of transition metal dichalcogenides (TMDCs)1,2. It originates from the strong spin-orbit interaction³, which arises from the heavy transition metals in TMDCs and the broken inversion symmetry of the crystal lattice. This leads to inverted spin orientations at opposite K points at the corners of the hexagonal Brillouin zone, for both conduction band electrons and valence band holes. As a result, the K and K' valleys can be selectively addressed by σ^+ and σ^- circularly polarized light^{4,5}, which is referred to as valley polarization. Likewise, coherent superpositions of both valleys can be excited by linearly polarized light, which is referred to as valley coherence. The precise control of the valley pseudospin has attracted great interest in exploiting this degree of freedom to encode and process information by manipulating free charge carriers⁶ and excitons⁷⁻⁹, which has led to the emerging field of valleytronics¹⁰. However, exciton spin-valley applications are strongly limited by the depolarization mechanisms due to the strong Coulomb exchange interaction of electrons and holes, as well as by the limited exciton diffusion and propagation lengths.

Thus far, in most experiments, TMDC monolayers were nonresonantly excited several hundreds of millielectronvolts above the ground state, so that excitons were created with a finite centre-ofmass wave vector¹¹. In this configuration, the long-range Coulomb exchange interaction of the exciton's constituent electron and hole creates an efficient depolarization mechanism^{12,13}. The eigenstates of excitons with their dipole orientation parallel to the wave vector (longitudinal exciton) and with their dipole orientation perpendicular to the wave vector (transverse exciton) are split in energy. This so called L–T splitting increases linearly with the centre-of-mass wave vector, and mixes the K and K' excitons, which ultimately leads to a depolarization of excitons during their energy relaxation ¹⁴.

One way to reduce this depolarization effect is to excite the system quasiresonantly close to the exciton transition energy. As a result, excitons are created with small in-plane wave vectors that correspond to a relatively small L–T splitting, and need to undergo less inelastic scattering events before their radiative decay (compared with non-resonantly excited excitons). This approach has been used to measure reasonably high degrees of circular polarization (DOCP) in MoS₂ (40%)¹⁵, WS₂ (90%)¹⁶ and WSe₂ (40%)¹⁷ monolayers at cryogenic temperatures and DOCP values up to 30% in a WS₂ monolayer at room temperature¹⁸. However, in MoSe₂ a DOCP of only a few per cent has been observed this way^{19,20}. To achieve close-to-unity valley polarization, excitons in WSe₂ have been resonantly excited in a two-photon absorption process²¹.

An alternative approach to enhance the valley polarization is the tailoring of the electrodynamic environment of the monolayer. This can be accomplished by the integration of a TMDC monolayer into an optical microcavity, resulting in the formation of exciton-polaritons (polaritons)^{20,22}. This approach has been used to increase the DOCP in MoS₂ and WS₂ monolayers at room temperature^{23–25} and to induce a significant valley polarization in MoSe₂ monolayers^{20,26} at cryogenic temperatures. Here, the strong coupling between the optical cavity mode and the monolayer exciton speeds up the energy relaxation and decay dynamics, which is beneficial for preserving the valley polarization^{20,23,26}. Moreover, intervalley scattering

¹Technische Physik and Wilhelm-Conrad-Röntgen-Research Center for Complex Material Systems, Universität Würzburg, Würzburg, Germany.

²Physics and Astronomy School, University of Southampton, Southampton, UK. ³Vladimir State University named after A.G. and N.G. Stoletovs, Vladimir, Russia. ⁴Univ. Grenoble Alpes, CNRS, Grenoble INP, Institute Neel, Grenoble, France. ⁵Ioffe Institute, St. Petersburg, Russia. ⁶Arizona State University, Tempe, AZ, USA. ⁷Westlake University, Hangzhou, China. ⁸Institute of Natural Sciences, Westlake Institute for Advanced Study, Hangzhou, China. ⁹Spin Optics Laboratory, St Petersburg State University, St Petersburg, Russia. ¹⁰SUPA, School of Physics and Astronomy, University of St Andrews, St Andrews, UK. *e-mail: christian.schneider@uni-wuerzburg.de

NATURE NANOTECHNOLOGY ARTICLES

is greatly suppressed in the strong coupling regime²⁰, owing to the strongly reduced disorder scatting of the photon component of the polariton²⁷. Polaritons in TMDC monolayers also have a much longer diffusion length than excitons in a bare monolayer^{28–30}, which should be a substantial advantage with respect to the spatial separation of valley-tagged excitations.

In this work, we make use of these two approaches to enhance valley polarization and valley coherence in a TMDC monolayer. First, we strongly couple excitons in an elongated MoSe₂ monolayer to the optical mode of a mechanically assembled high-quality (Q)-factor microcavity. Next, we excite the exciton-polariton states quasiresonantly close to their ground state by a two-photon absorption process. Combining both approaches enables us to generate valley polarization and valley coherence of the quasiparticles with circular and linear polarization degrees exceeding 90%. The ultimate control over valley polarization and valley coherence is key for observing the optical valley Hall effect (OHVE): polaritons with opposite valley indices propagate in different directions, resulting in the valley separation of exciton-polaritons, analogous to spin-up and spin-down electrons in a semiconductor driven by an external electric field³¹. We demonstrate this effect by studying the polarization of polaritons expanding along the monolayer. The spin-Hall phenomenology in optical distributed Bragg reflector (DBR) cavities, which is translated to the valley Hall physics in chiral valley monolayers, arises from the splitting of the transverse electric and transverse magnetic modes at finite in-plane wave vectors³². This is qualitatively similar to the L-T splitting of excitons, but the transverse electric-transverse magnetic splitting is approximately two orders of magnitude larger²⁷. Thus, if excitons strongly couple to a microcavity photon mode and propagate with finite velocities, the emergent polaritons experience a spin-dependent propagation³². In our sample, this is manifested in a clearly observed and closely controllable spatial separation of valley-tagged polaritons, which is a clear-cut feature of the OVHE27.

Sample structure and polariton formation

The studied sample structure is schematically depicted in Fig. 1a. The mechanically assembled microcavity is built by transferring a MoSe₂ monolayer onto a SiO₂/TiO₂ bottom DBR (10 pairs, stop band centre at 750 nm) with a dry-gel method³³. The monolayer was mechanically exfoliated from a bulk crystal. We then spin-coated a 126-nm-thick polymethyl methacrylate (PMMA) buffer layer. Finally, a piece of a separate SiO₂/TiO₂ DBR with lateral dimensions of a few tens of micrometres (8.5 pairs, stop band centre at 750 nm) is mechanically peeled off its substrate. This piece is transferred onto the buffer layer with the same dry-gel method³³. Van der Waals forces are sufficiently strong to keep the top DBR in place. We found that such microcavities demonstrate Q factors up to 4,600 (see Supplementary Section 1). Figure 1b shows a microscope image of the final structure (top view), in which the MoSe₂ monolayer (8×40 µm²) is marked in blue. A photoluminescence spectrum of the monolayer capped with PMMA was taken at 5 K (Fig. 1c) before the microcavity was completed with the top DBR. The monolayer exhibits a neutral exciton resonance at 745.5 nm/1.663 eV and a charged exciton (trion) resonance at 759.8 nm/1.632 eV. Figure 1c also shows a reflectivity spectrum of the uncoupled cavity mode at 747.3 nm/1.659 eV, measured close to the monolayer.

First, we probe the in-plane-momentum-resolved photoluminescence of the full structure at the monolayer position at 5 K under continuous-wave excitation with a titanium:sapphire laser (Msquared SolsTiS) at 740 nm. Neither the cavity mode, nor exciton or trion can be observed, but a new mode appears with a ground state at 761.4 nm/1.628 eV, as presented in Fig. 1d. This mode has a parabolic dispersion at small in-plane-momentum components parallel to the long axis of the monolayer. In contrast, if the dispersion is measured perpendicular to the monolayer extension, discrete levels

appear in the photoluminescence spectrum (depicted in Fig. 1e). The mode splitting of 2.7 meV between the fundamental and first excited modes is fully consistent with an optical mode confinement caused by the monolayer width of 8 µm (see Supplementary Section 5). We attribute this new mode to the lower polariton branch of the strongly coupled exciton-cavity system. The upper polariton branch (and likewise, the lower polariton states with large in-plane wave vectors) are typically not observed in photoluminescence spectra acquired under non-resonant pumping, as the thermal population of polaritons can be very low at cryogenic temperatures³⁴. To provide further evidence for the formation of exciton-polaritons, that is the strong light-matter coupling regime, we have carried out two-photon excitation experiments (Supplementary Section 2), magnetic field measurements (Supplementary Section 3) and white-light reflection measurements at various temperatures (see Supplementary Section 4). On the basis of these measurements, we modelled the presented lower polariton dispersion using a twocoupled-oscillator model, which yielded a normal mode splitting of 46 meV and an exciton fraction of 26% in the ground state (see Supplementary Section 2). The two-coupled-oscillator model is also presented as an overlay to the measured dispersion in Fig. 1d.

TMDC monolayers can be excited under two-photon absorption²¹, which originates from a two-photon interband transition and also gives rise to the second-harmonic-generation (SHG) process^{35,36}. This strong nonlinear response is transferred to our strongly coupled system³⁷ and thus provides an ideal setting for studying polaritons under nearly resonant excitation conditions. This allows us to directly address polaritons arising from specific valleys of the embedded crystals via quasiresonant chiral two-photon absorption. Clean, high-fidelity excitation of valley polaritons is necessary for studies of exciton-polaritons in valleytronic experiments. Here, we excite our system at 5 K with 2 ps laser pulses at 1,518 nm (Coherent Mira-OPO system, 76 MHz repetition rate) with circular polarization of the spin-up (σ^+) and spin-down (σ^-) states and analyse the polarization of the emitted light (Fig. 2a). The measured spectra for σ^+ and σ^- excitations are plotted in Fig. 2b and c, respectively. We observe that the emitted signal is strongly polarized with an opposite helicity to the polarization of excitation. The observation of a counter-rotating signal is fully consistent with SHG selection rules for crystals with broken inversion symmetry and a three-fold rotation symmetry³⁸, and likewise for two-photon active interband transitions^{21,35}. In Fig. 2b,c, we plot the degree of circular polarization of the emission across the acquired spectrum, including genuine second-harmonic signals and luminescence following the two-photon absorption process (more details on the distinction of SHG versus two-photon-induced photoluminescence are given in Supplementary Sections 6, 7 and 9). We find that a valley polarization of more than 90%, as demonstrated by the corresponding DOCP, is preserved even at energies that are well below the second-harmonic resonance, which is characteristic for two-photoninduced photoluminescence^{21,36}. The outstandingly high valley polarization is explained by two factors: first, the excited polariton states are situated close to the ground state, and their in-plane wave vectors are therefore low (<1.5 µm⁻¹). Hence, the transverse electric-transverse magnetic splitting of the cavity and the renormalizations of the exciton oscillator strengths in L and T polarizations (the two main mechanisms of the depolarization) are small compared with those for non-resonant excitation. Second, the polariton lifetime is shortened to about 200 fs by coupling to the cavity (see Supplementary Section 8) rather than the pure excitons in MoSe₂ monolayer (390 fs; ref. 39). As assessed in earlier work 20,27, the strong coupling conditions further mitigate the influence of strong exciton localization and disorder scattering, as the spatial extent of the polaritonic wavefunction is much greater than typical excitonic disorder in the monolayer. This enables valley-polariton relaxation timescales that are extended by a factor of approximately 20. The ARTICLES NATURE NANOTECHNOLOGY

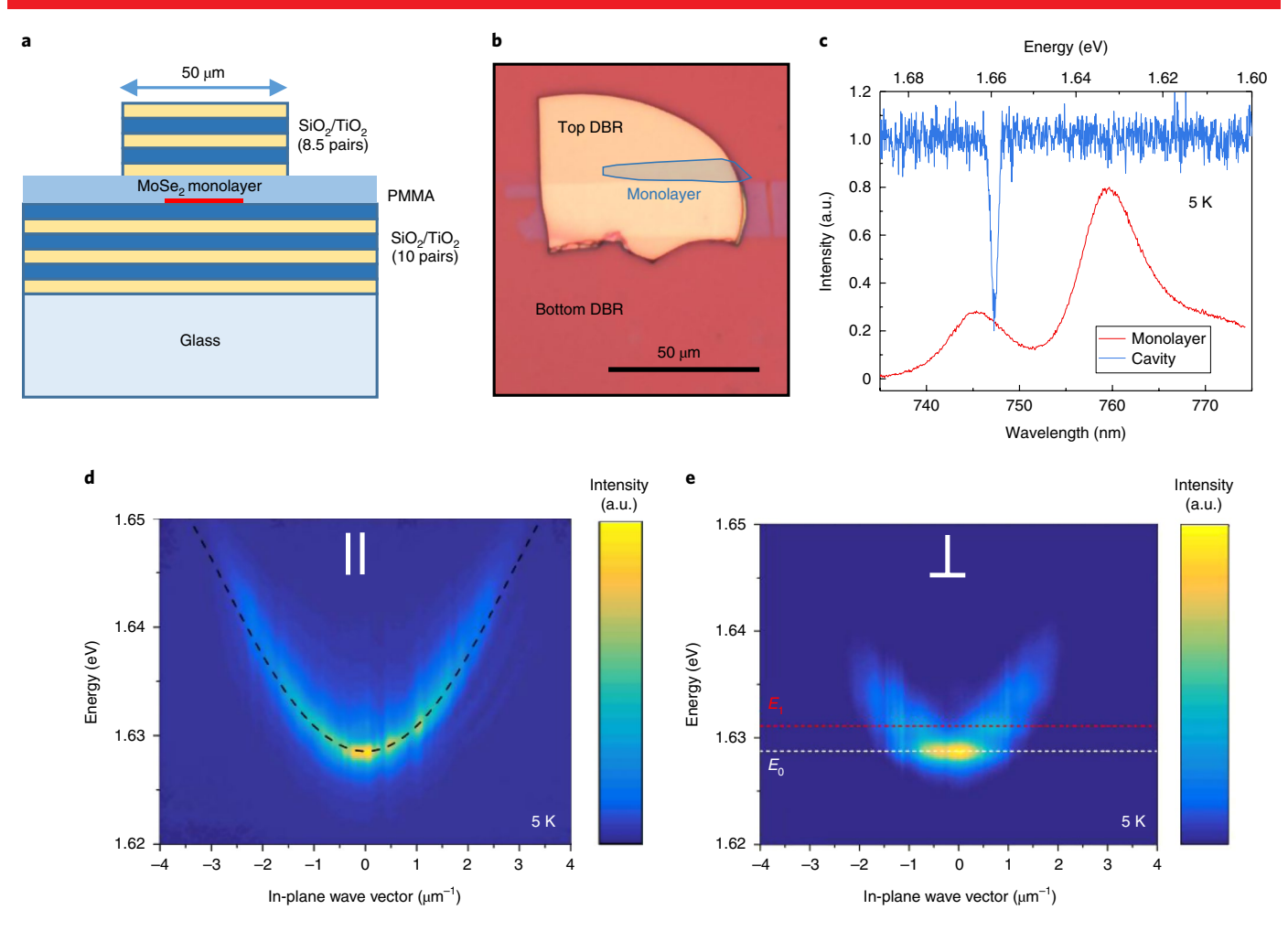


Fig. 1 | Sample design and characterization. **a**, Sketch of the mechanically assembled microcavity. **b**, Optical image of the cavity and the elongated monolayer, which provides the channel geometry. **c**, Photoluminescence measurement of the untreated monolayer and the reflectivity of the optical empty-cavity resonance at 5 K. **d**,**e**, Momentum-resolved photoluminescence spectrum recorded at 5 K along the stripe direction (**d**) and perpendicular to the stripe (**e**). In **d**, the measurement is overlaid with a two-coupled-oscillator model (dashed curve), presented in Supplementary Section 2. In **e**, the mode discretization (which arises from the finite monolayer width of 8 μm) is marked for the first (white) and second (red) discretized states.

negative detuning of the exciton and cavity photon mode is crucial for such suppression of disorder scattering 27 , a strong increase in the degree of circular polarization can therefore be expected in our resonantly driven cavity polariton system. The resulting DOCP is governed by the interplay between the radiative decay time τ and spin-valley relaxation time $\tau_{\rm s}$, and can be approximated

by
$$\rho_{\rm circ}=
ho_0/\Big(1+rac{ au}{ au_{\rm s}}\Big)$$
 (refs. ^{11,24}), where ho_0 is the initial polarization

(close to 100%) and $\rho_{\rm circ}$ is the resulting DOCP in the luminescence. The spin-valley relaxation time for the pure MoSe₂ monolayer exciton is 150 fs (refs. ^{20,39}), resulting in a polariton $\tau_{\rm s}$ of 3 ps (ref. ²⁰). From these values, we calculate a valley polarization of 94%, which is in excellent agreement with our experimental observations.

Valley polaritons can be generated by exciting with circularly polarized light, as shown above, whereas excitation with linearly polarized light may induce a coherent superposition of valley polaritons. Valley coherence up to 80% has been observed in bare monolayers of MoS_2^{40} , WS_2^{18} and WSe_2^{41} , but has not been measured in $MoSe_2$. For our valley polaritons, the degree of linear polarization (DOLP) ρ_{lin} of the decaying polariton field provides a direct measure of the dephasing processes of the polariton pseudospin vector on the equator of the Bloch sphere (Fig. 2d). We probe our system by exciting at 1,514 nm (757 nm) with linearly polarized light in the

X and *Y* directions, where the *X* axis is aligned with one of the crystal axes (see Supplementary Section 6 and 9 for crystal axis alignment) and the Y axis is perpendicular to the X axis. The emitted signal I(X), respectively I(Y), is subsequently measured in the same axis and the DOLP was determined by $\rho_{\text{lin}} = \frac{I(X) - I(Y)}{I(X) + I(Y)}$. Figure 2e,f shows the acquired spectra, along with the calculated DOLP as a function of the detection wavelength. The polarization of the resonantly scattered fraction of the signal (the SHG portion) is expected to be fully governed by the crystal symmetry and yields no information about the valley coherence of the polaritons (see Supplementary Section 9 for SHG selection rules). However, it should be noted that a strong linear polarization is maintained in the broad two-photon-induced photoluminescence emission of the polariton resonances, even 10 meV below the energy of the SHG signal, with a DOLP clearly exceeding 90% close to the polariton ground state. The DOLP thus clearly reflects the valley coherence.

The phase of the coherent valley superposition can be addressed by changing the direction of the linear polarization of the pump beam. In Fig. 2f, we show that the two-photon-induced-photoluminescence retains the direction of the linear polarization of the pump oriented along the *Y* direction, and therefore allows us to extract large degrees of valley coherence exceeding 90% even 10 meV below the SHG frequency. In contrast, the DOLP signal is close to zero

ARTICLES

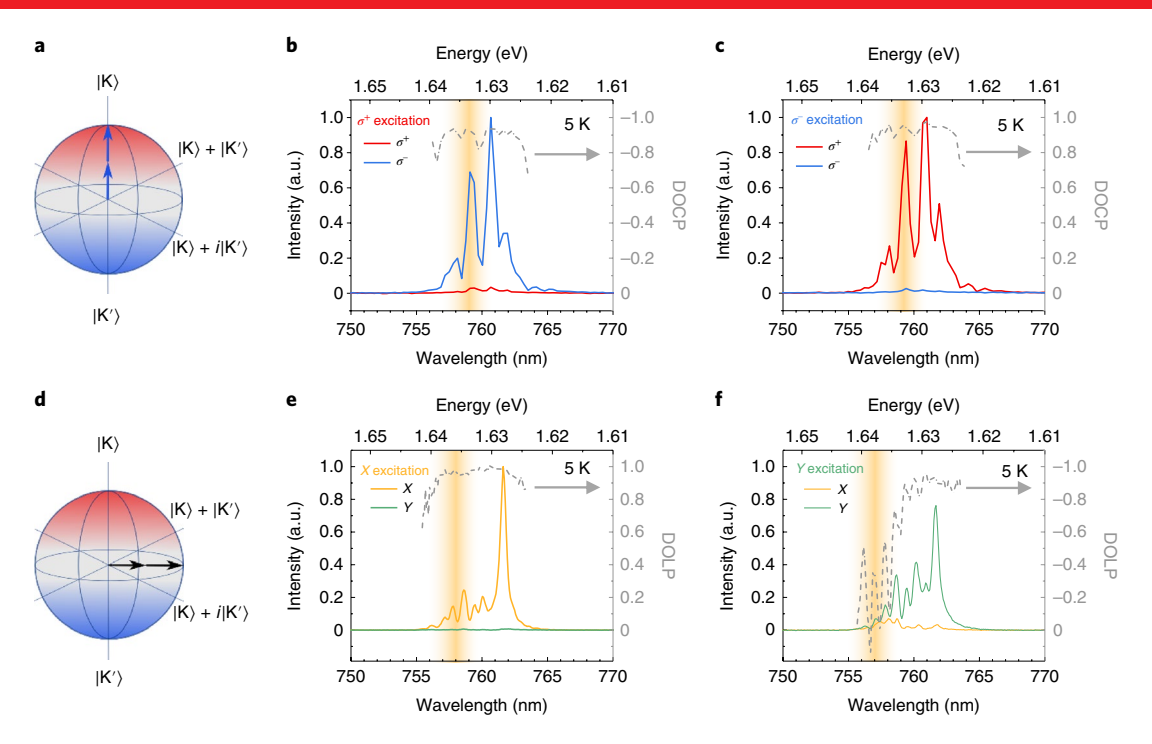


Fig. 2 | Valley polarization and coherence of polaritons. a, Schematic of the polariton pseudospin, which is generated at K/K' by quasiresonant two-photon absorption. **b,c**, Polarization-resolved emission spectra of polaritons excited at 5 K by a σ^+ polarized near-infrared laser (**b**) and σ^- polarized laser (**c**). The DOCP of the emitted signals (right y axis) reveal a strongly counterpolarized emission. The energy of the second-harmonic resonance is indicated by the orange shading. **d**, Schematic of the excitation of a valley-coherent state, which is generated by quasiresonant two-photon absorption. **e,f**, Polarization-resolved emission spectra of polaritons excited at 5 K with a linearly polarized near-infrared laser along X (**e**) and linear polarized injection along Y (**f**). The DOLP of the emitted signals (right y axis) reveal a strongly copolarized emission. The energy of the SHG resonance is indicated by the orange shading.

or even negative around the SHG frequency, due to the specific SHG selection rules in the TMDC monolayer³⁵ (see Supplementary Section 9 for details).

Although near-unity valley polarization has been observed on bare WSe₂ monolayers²¹, the degrees of valley coherence demonstrated here in an MoSe₂ monolayer clearly outline the potential of strong light–matter coupling for the generation and manipulation of coherent valley superposition states in hybrid light–matter quasiparticles.

The optical valley Hall effect

In contrast to TMDC excitons, which have a diffusion length of a few hundred nanometres in high-quality samples^{29,30}, TMDC-based polaritons are expected to expand over significantly longer distances (on the order of 10 µm) even in the linear, non-superfluid regime due to their small effective masses²⁸. Figure 3a depicts the spatial intensity distribution of near-resonantly injected polaritons on the monolayer at 5 K. From this intensity distribution, we can infer that our polaritons propagate by approximately 3.6 µm before they decay (see Supplementary Section 10). It should be noted that an excitation slightly above the ground state of the lower polariton branch (in this case 10 meV) is essential to create polaritons with finite wave vectors and velocities. Such long propagation distances allow us to investigate the valley-dependent polariton propagation following valley-coherent initialization of the system. This is recorded via spatial- and polarization-resolved luminescence. Here, the σ^+ and σ^- polarized components of the emission were measured as a function of position (see Methods), and the spatially resolved DOCP was deduced. Figure 3b depicts a DOCP distribution recorded under linearly polarized two-photon excitation at 1,514 nm. The initial polarization angle was -75° with respect to the long axis of the monolayer. The DOCP distribution clearly shows two domains

with a left–right separation that is slightly rotated clockwise and features an oscillating pattern along the vertical stripe direction. As we rotate the orientation of the initial polarization by -45° (Fig. 3c), we observe a dramatic change in the polarization pattern with a vertical domain separation and weak σ^+ regions along the right edge of the monolayer. We note that similar patterns have been predicted³² and observed^{42,43} as spin domains of exciton-polaritons in GaAs quantum wells embedded in microcavities, known as the optical spin Hall effect^{32,42}. In contrast to GaAs, the spin and valley indices cannot be treated separately in TMDC monolayer excitons and, consequently, the valley-dependent expansion of polaritons leads to the emergence of the OVHE²⁷.

The intensity and DOCP distributions were modelled for the measured monolayer geometry and the experimental conditions based on the physics of the OVHE effect. The details of the model can be found in the Methods and Supplementary Sections 11–13. The simulated intensity distribution (plotted in Fig. 3d) shows a polariton propagation tail along the monolayer that is similar to the experimentally observed one. The simulated DOCP distributions, calculated as $\left(|\psi_+|^2-|\psi_-|^2\right)/\left(|\psi_+|^2+|\psi_-|^2\right)$, for the same initial linear polarization orientations that were used in the experiments are plotted in Fig. 3e and f, respectively. Here, ψ_+ and ψ_- are the wavefunctions of the right and left circularly polarized polariton components.

For an initial polarization angle of -75° with respect to the long axis of the monolayer, the simulation closely reproduces the valley separation. As in the experiment, the DOCP increases towards the edges of the flake. Polaritons that decay further away from the excitation spot are associated with higher in-plane wave vectors, which in turn provide higher splittings and stronger effective magnetic fields. The precession of the pseudospin (which is equivalent to the

ARTICLES NATURE NANOTECHNOLOGY

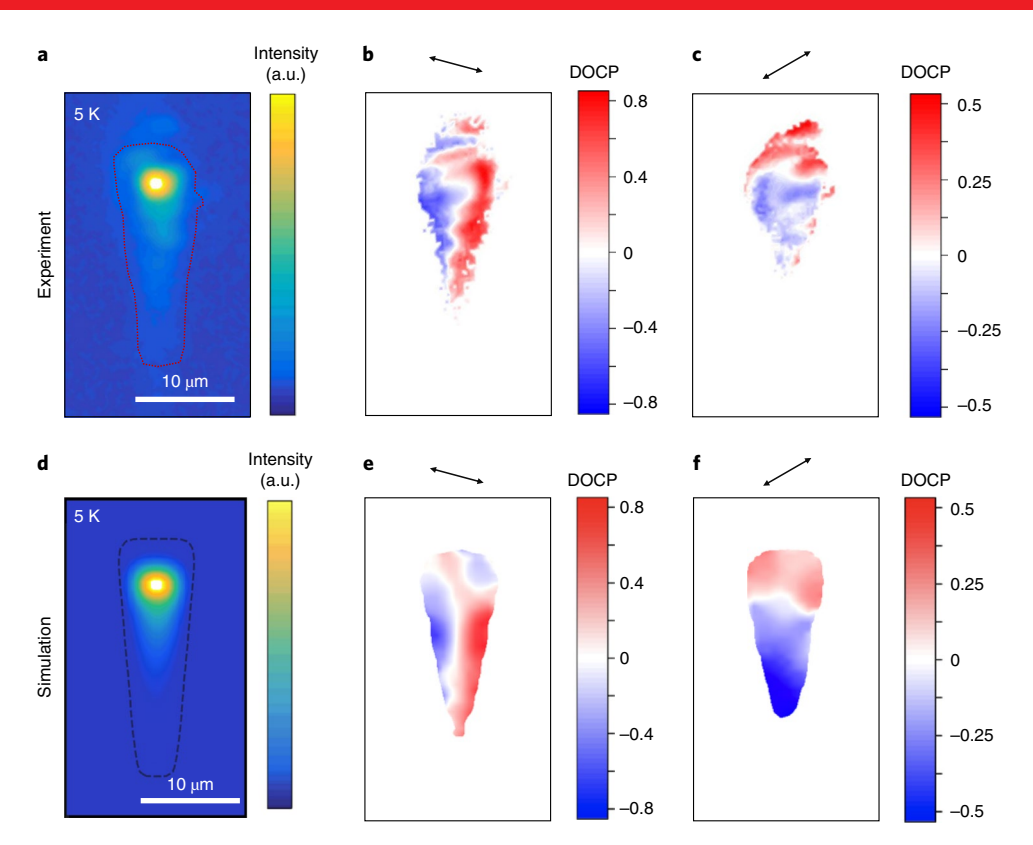


Fig. 3 | Optical valley Hall effect. a, Photoluminescence intensity distribution along the monolayer observed under two-photon excitation at 1,514 nm. The white point marks the excitation spot on the monolayer and the edge of the monolayer is indicated by the dotted line. **b**, Spatially resolved DOCP distribution across the monolayer. The polarization orientation of the excitation light (–75° with respect to the long axis of the monolayer) is indicated by the double-headed arrow. **c**, Spatically resolved DOCP distribution across the monolayer with a polarization orientation that was rotated by –45° (–120° with respect to the long axis of the monolayer). **d-f**, The corresponding intensity and DOCP distributions of the simulation.

polarization Stokes vector) is consequently more pronounced, leading to a larger valley polarization. Moreover, the wavy domain separation line is also clearly seen in the simulation. This is explained by interfering polaritons that are reflected at the monolayer edges. The simulation of the rotated initial polarization in Fig. 3f is again in good qualitative agreement with our experimental data. The main, bottom section of the monolayer is strongly dominated by a σ^- domain with small σ^+ regions at the right edge of the monolayer. Further experimental data, which were recorded at intermediate excitation angles, support our assignment to the OVHE, and can be found in Supplementary Section 14.

The very good agreement of our experimental data with the theoretical modelling allows us to interpret our experimental data as the first manifestation of the OVHE in a TMDC exciton-polariton system. We note that our experimentally observed valley polarized domains yield DOCP up to 80%, which itself is a remarkable consequence of the strong valley polarization and valley coherence, which are preserved by our experimental approach (see Supplementary Section 15 for comparative measurements taken via linear spectroscopy).

Conclusion

We have demonstrated that near-unity valley polarization and valley coherence can be achieved under near-resonant two-photon excitation by integrating a TMDC monolayer into a high-Q microcavity. Such high degrees of circular and linear polarization are facilitated by the strong coupling conditions, which simultaneously reduce the radiative lifetime of the quasiparticle and prolong the depolarization time at states close to the polariton

ground state. Taking advantage of these conditions, we have studied the valley-dependent, optically controllable propagation of exciton-polaritons. Clear signatures of polarization domains emerge in the expansion of polaritons, as observed in the valley-coherent excitation scheme. This is a characteristic of the OVHE that allows us to observe the interplay of the spin, valley and momentum of our quasiparticles, driven by internal pseudomagnetic fields.

The combination of two-photon excitation and cavity quantum electrodynamics allows us to reach a high degree of valley control, even in MoSe, monolayers, which are known to exhibit a poor DOCP as bare monolayer²⁰. It has been argued that the presence of a low-lying dark exciton state in tungsten-based TMDC materials, which is not subject to the exchange-induced depolarization mechanism, is beneficial for the observation of large degrees of valley polarization and coherence44. Thus, we suspect that similar experiments with even more pronounced degrees of polarization could be successful with high-quality, tungsten-based TMDC layers, potentially also at elevated temperatures. Although the OVHE of propagating polaritons may be utilized in valleytronic on-chip applications, the interplay of valley-coherent superpositions and photonic spin-orbit coupling⁴⁵ could be exploited to harness valley-path entanglement phenomena of propagating quantum wavepackets of polaritons. Likewise, by carefully preparing monolayers with imprinted superpotentials for excitons, similar experiments could demonstrate topologically non-trivial expanding polaritons in a similar framework⁴⁶, and even pave the way towards topological lasers based on TMDC crystals in the strong coupling regime⁴⁷.

NATURE NANOTECHNOLOGY ARTICLES

Online content

Any methods, additional references, Nature Research reporting summaries, source data, statements of code and data availability and associated accession codes are available at https://doi.org/10.1038/s41565-019-0492-0.

Received: 6 August 2018; Accepted: 3 June 2019; Published online: 22 July 2019

References

- 1. Xiao, D. et al. Coupled spin and valley physics in monolayers of MoS_2 and other group-VI dichalcogenides. *Phys. Rev. Lett.* **108**, 196802 (2012).
- Xu, X., Yao, W., Xiao, D. & Heinz, T. F. Spin and pseudospins in layered transition metal dichalcogenides. Nat. Phys. 10, 343–350 (2014).
- 3. Dyakonov, M. I. Spin Physics in Semiconductors (Springer, 2008).
- Mak, K. F., He, K., Shan, J. & Heinz, T. F. Control of valley polarization in monolayer MoS, by optical helicity. *Nat. Nanotechnol.* 7, 494–498 (2012).
- Cao, T. et al. Valley-selective circular dichroism of monolayer molybdenum disulphide. Nat. Commun. 3, 885–887 (2012).
- Mak, K. F., McGill, K. L., Park, J. & McEuen, P. L. The valley Hall effect in MoS, transistors. Science 344, 75–79 (2014).
- Onga, M., Zhang, Y., Ideue, T. & Iwasa, Y. Exciton Hall effect in monolayer MoS₂. Nat. Mater. 16, 1193–1198 (2017).
- Wang, G. et al. Control of exciton valleycoherence in transition metal dichalcogenide monolayers. *Phys. Rev. Lett.* 117, 187401 (2016).
- Ye, Z., Sun, D. & Heinz, T. F. Optical manipulation of valley pseudospin. Nat. Phys. 13, 26–30 (2017).
- Schaibley, J. R., Yu, H., Yao, W. & Xu, X. Valleytronics in 2D materials. Nat. Rev. Mater. 1, 16055 (2016).
- Wang, G. et al. Colloquium: excitons in atomically thin transition metal dichalcogenides. Rev. Mod. Phys. 90, 21001 (2018).
- Glazov, M. M. et al. Exciton fine structure and spin decoherence in monolayers of transition metal dichalcogenides. *Phys. Rev. B* 89, 201302 (2014).
- Glazov, M. M. et al. Spin and valley dynamics of excitons in transition metal dichalcogenide monolayers. *Phys. Stat. Solidi* 252, 2349–2362 (2015).
- Maialle, M. Z., Silva, E. & Sham, L. J. Exciton spin dynamics in quantumwells. Phys. Rev. B 47, 15776 (1993).
- Kioseoglou, G., Hanbicki, A. T., Currie, M., Friedman, A. L. & Gunlycke, D. Valley polarization and intervalley scattering in monolayer MoS₂. Appl. Phys. Lett. 101, 221907 (2012).
- Zhu, B., Zeng, H., Dai, J., Gong, Z. & Cui, X. Anomalously robust valley polarization and valley coherence in bilayer WS₂. *Proc. Natl Acad. Sci. USA* 111, 11606–11611 (2014).
- Jones, A. M. et al. Optical generation of excitonic valley coherence in monolayer WSe₂. Nat. Nanotechnol. 8, 6–10 (2013).
- Hanbicki, A. T. et al. Anomalous temperature-dependent spin-valley polarization in monolayer WS₂. Sci. Rep. 6, 18885 (2016).
- Wang, G. et al. Polarization and time-resolved photoluminescence spectroscopy of excitons in MoSe₂ monolayers. *Appl. Phys. Lett.* 106, 112101 (2015).
- Dufferwiel, S. et al. Valley-addressable polaritons in atomically thin semiconductors. *Nat. Photon.* 11, 497–501 (2017).
- Seyler, K. L. Electrical control of second-harmonic generation in a WSe₂ monolayer transistor. *Nat. Nanotechnol.* 10, 1–5 (2015).
- Dufferwiel, S. et al. Valley coherent exciton-polaritons in a monolayer semiconductor. *Nat. Commun.* 9, 4797 (2018).
- Chen, Y., Cain, J. D., Stanev, T. K., Dravid, V. P. & Stern, N. P. Valleypolarized exciton-polaritons in a monolayer semiconductor. *Nat. Photon.* 11, 431–435 (2017).
- 24. Sun, Z. et al. Optical control of room-temperature valley polaritons. *Nat. Photon.* **11**, 491–496 (2017).
- Lundt, N. et al. Observation of macroscopic valley-polarized monolayer exciton-polaritons at room temperature. Phys. Rev. B 96, 241403 (2017).
- Lundt, N. et al. Valley polarized relaxation and upconversion luminescence from Tamm-plasmon trion-polaritons with a MoSe₂ monolayer. 2D Mater. 4, 25096 (2017).
- Bleu, O., Solnyshkov, D. D. & Malpuech, G. Optical valley Hall effect based on transitional metal dichalcogenide cavity polaritons. *Phys. Rev. B* 96, 165432 (2017).
- Barachati, F. et al. Interacting polariton fluids in a monolayer of tungsten disulfide. Nat. Nanotechnol. 13.10, 906 (2018).
- Kulig, M. et al. Exciton diffusion and halo effects in monolayer semiconductors. *Phys. Rev. Lett.* 120, 207401 (2018).

- Cadiz, F., Paget, D., Urbaszek, B. & Marie, X. Exciton diffusion in WSe₂ monolayers embedded in a van der Waals heterostructure. *Appl. Phys. Lett.* 112, 152106 (2018).
- 31. Dyakonov, M. I. & Perel, V. I. Current-induced spin orientation of electrons in semiconductors. *Phys. Lett.* **35**, 1–2 (1971).
- Kavokin, A., Malpuech, G. & Glazov, M. Optical spin Hall effect. Phys. Rev. Lett. 95, 136601 (2005).
- Castellanos-Gomez, A. et al. Deterministic transfer of two-dimensional materials by all-dry viscoelastic stamping. 2D Mater. 1, 11002 (2014).
- Kulakovskii, V. D. et al. Bose–Einstein condensation of exciton polaritons in high Q planar microcavities with GaAs quantum wells. *JETP Lett.* 92, 595–599 (2010).
- Glazov, M. M. et al. Intrinsic exciton-state mixing and nonlinear optical properties in transition metal dichalcogenide monolayers. *Phys. Rev. B* 95, 35311 (2017).
- Wang, G. et al. Exciton states in monolayer MoSe₂: impact on interband transitions. 2D Mater. 2, 45005 (2015).
- Schmutzler, J. et al. Nonlinear spectroscopy of exciton-polaritons in a GaAs-based microcavity. Phys. Rev. B 90, 1–6 (2014).
- Simon, H. J. & Bloembergen, N. Second-harmonic light generation in crystals with natural optical activity. *Phys. Rev.* 171, 1104–1114 (1968).
- Jakubczyk, T. et al. Radiatively limited dephasing and exciton dynamics in MoSe₂ monolayers revealed with four-wave mixing microscopy. *Nano Lett.* 16, 5333–5339 (2016).
- Cadiz, F. et al. Excitonic linewidth approaching the homogeneous limit in MoS₂-based van der Waals heterostructures. *Phys. Rev. X* 7, 21026 (2017).
- Wang, G. et al. Giant enhancement of the optical second-harmonic emission of WSe₂ monolayers by laser excitation at exciton resonances. *Phys. Rev. Lett.* 114, 97403 (2015).
- Leyder, C. et al. Observation of the optical spin Hall effect. Nat. Phys. 3, 628–631 (2007).
- Maragkou, M. et al. Optical analogue of the spin Hall effect in a photonic cavity. Opt. Lett. 36, 1095–1097 (2011).
- 44. Baranowski, M. et al. Dark excitons and the elusive valley polarization in transition metal dichalcogenides. 2D Mater. 4, 025016 (2017).
- 45. Manni, F. et al. Spin-to-orbital angular momentum conversion in semiconductor microcavities. *Phys. Rev. B* **83**, 241307 (2011).
- 46. Huang, S. et al. Topologically protected helical states in minimally twisted bilayer graphene. *Phys. Rev. Lett.* **121**, 37702 (2018).
- 47. Klembt, S. et al. Exciton-polariton topological insulator. *Nature* **562**, 552–556 (2018).

Acknowledgements

C.S. acknowledges support from the ERC (Project unLiMIt-2D). The Würzburg group acknowledges support from the State of Bavaria. A.V.K. acknowledges support from Westlake University (Project No. 041020100118). A.V.K. acknowledges the St Petersburg State University for research grant ID 40847559. E.S. acknowledges support from the Grant of the President of the Russian Federation for state support of young Russian scientists No. MK-2839.2019.2 and RFBR Grant No. 17-52-10006. S.K. acknowledges support from the EU (Marie Curie Project TOPOPOLIS). Q.Y. and S.T. acknowledge funding from NSF DMR-1838443 and DMR-1552220. M.M.G. acknowledges partial support from RFBR Project No. 17-02-00383.

Author contributions

N.L. exfoliated, identified and transferred the monolayer and designed and fabricated the microcavity. Y.Q. and S.T. synthesized the bulk crystal. N.L., Ł.D., S.K., M.K. and P.S. performed experiments. N.L., S.K., M.K., J.B., M.R. and C.S. analysed and interpreted the experimental data, supported by all co-authors. E.S., M.M.G. and A.V.K. provided the theory. N.L. and C.S. wrote the manuscript, with input from all co-authors. C.S. and S.H. initiated the study and guided the work.

Competing interests

The authors declare no competing interests.

Additional information

Supplementary information is available for this paper at https://doi.org/10.1038/s41565-019-0492-0.

Reprints and permissions information is available at www.nature.com/reprints.

Correspondence and requests for materials should be addressed to C.S.

Publisher's note: Springer Nature remains neutral with regard to jurisdictional claims in published maps and institutional affiliations.

© The Author(s), under exclusive licence to Springer Nature Limited 2019

ARTICLES NATURE NANOTECHNOLOGY

Methods

Experimental set-up. We used an optical set-up in which both spatially (nearfield) and momentum-space- (far-field) resolved spectroscopy and imaging are accessible. Various laser sources could be coupled into the beam path, including a 532 nm CW laser, a wavelength tuneable CW laser (700-980 nm), and a wavelength tuneable system composed of a Titanium Saphire laser (2 ps pulse length) which is driving an optical parametric oscillator (tuning range 1100-1600 nm). We used a thermal light-source to image the sample, as well as for white-light reflection spectroscopy. The light was then directed through a microscope objective (0.65 NA) onto the sample, which was mounted in a liquid Helium cryostat (temperature down to 4.2 K). Using the objective allows a sample to be probed with a focus spot diameter of 2 µm for the laser excitation and 10 µm for the whitelight illumination. The re-emitted or reflected light is collected by the objective and propagates through a lens system to the entrance plane of the spectrometer. Our setting allowed us to access both the spatial and angular distribution of the emitted signal from the sample. To obtain a spatially resolved signal, the emission from the sample was simply projected onto the imaging plane of the spectrometer in a conventional microscope configuration. To switch to the angle-resolved configuration, an additional lens was placed into the beam path, where its distance to the back focal plane of the objective was equivalent to its focal length. This configuration is also known as Fourier space imaging, which allows imaging of the angular distribution of the emitted light onto the Peltier-cooled CCD (chargecoupled device) camera of the spectrometer. The angular resolution of the system is ~0.03 μm⁻¹ (~0.2°). A second closed-cycle cryostat providing magnetic fields up to 9T and sample temperatures down to 1.8K was integrated into the set-up. In this setting, the photoluminescence is collected through a 0.81 NA microscope objective for the magnetic field measurements. Both the real-space and Fourierspace configurations create an image in the focal plane of the spectrometer system. In the spectrometer, this plane is projected onto the CCD chip with two different options. For the first option, a slit in the entrance plane is closed to cut out a narrow section of the image in the y direction. The emitted signal is dispersed by an optical grating with either 150, 600 or 1,200 lines mm⁻¹ and energy resolutions of 1.1, 0.26 and 0.11 meV (at 750 nm), respectively. Ultimately, the CCD chip acquires a dataset that carries the spectral information along the x axis and either spatial position or emission angle along the y axis. Alternatively, the slit can be completely opened, the grating aligned to act like a mirror (zero-order reflection) and the CCD camera is then used to acquire an energy-averaged image of the emission. In this way, the CCD chip captures the full real-space or Fourier-space image.

To probe the sample with a well-defined polarization state, a linear polarizer is placed in the excitation path. Subsequently, either a commercial quarter- or half-wave plate are inserted. In the appropriate orientation, the quarter-wave plate induces a phase shift of $\frac{\pi}{2}$ and converts linearly polarized light to circularly polarized light (and vice versa). The half-wave plate induces a phase shift of π , which alters the orientation of the linearly polarized light. As all optical components can, in principle, affect the state of the incident light, a nominally non-polarizing beam splitter, objective and cryostat glass were used. Finally, a polarimeter (Schaefter-Kirchoff SK010PA) was used to quantify the actual polarization state of the incident light at the position where the sample is placed. In this manner, the orientations of the wave plates can be slightly corrected to compensate for the polarizing effect of the optical components' beam splitter. As a result, a degree of circular polarization of more than 99% in front of the cryostat window can be prepared. In the detection path, the emitted light is analysed with respect to its polarization. A quarter-wave plate is therefore inserted and oriented in such a way that σ^+ is converted to linear polarized light in the V orientation and σ is converted into the H orientation. Then, a linear polarizer is inserted, which transmits all V components and blocks all H components. Analogously, the quarter-wave plate is rotated to measure the intensity of the σ^- component.

It should be noted that all polarization optics were placed before the first mirror in the detection path, which may have an impact on the polarization state. The linear polarizer in the detection is also always kept at the same orientation, as the sensitivity of the spectrometer depends on the polarization of the detected light.

Model. We describe our system by solving the generalized Gross–Pitaevskii equation for the two-component wavefunction $\psi_{\sigma}(\mathbf{r},t)$ ($\sigma = \pm$)

$$\mathrm{i}\hbar\partial_t\psi_\sigma=\left[\hat{E}+V(\mathbf{r},t)\right]\!\psi_\sigma+\frac{\Delta}{2}\left(\hat{k}_x-\sigma\mathrm{i}\hat{k}_y\right)^2\!\psi_{-\sigma}+\mathrm{i}\frac{\hbar}{2}\left(Rn_\mathrm{R}^\sigma-\gamma\right)\!\psi_\sigma+P_\sigma(\mathbf{r},t)$$

coupled to the rate equation for the density of the spin-resolved reservoir of incoherent excitons $n_n^{\sigma}(\mathbf{r},t)$:

$$\partial_t n_{\rm R}^{\sigma} = \zeta |P_{\sigma}(\mathbf{r},t)|^2 - \left[\gamma_{\rm R} + R|\psi_{\sigma}|^2\right] n_{\rm R}^{\sigma}$$

where \hat{E} is the polariton kinetic energy operator, which reproduces the non-parabolic polariton dispersion in Fig. 1d observed experimentally and fitted using the two-coupled-oscillator model (see Supplementary Section 2); $V(\mathbf{r},t) = V_0(\mathbf{r}) + \alpha |\Psi_{\sigma}|^2 + \alpha_R n_R^{\sigma}$ is the effective potential experienced by polaritons. It consists of the stationary confinement potential across the sample $V_0(\mathbf{r})$ and the blueshift induced by polariton-polariton interactions within the condensate and interactions of polaritons with excitons in the incoherent reservoir. α and α_R are the corresponding interaction constants; $\alpha = X^2 \alpha_R$, where X^2 is the exciton fraction in the polariton state (to minimize the number of parameters, we neglected the effect of the oscillator strength saturation); Δ is the transverse electric–transverse magnetic splitting constant, $\hat{k} = (\hat{k}_x, \hat{k}_y) = (-i\partial_x, -i\partial_y)$ is the quasimomentum operator. The polariton condensate is excited by the non-homogeneous resonant optical pump $P_{\sigma}(\mathbf{r},t)$. To account for the inevitable appearance of the reservoir of incoherent excitons under the resonant pumping, we introduce the term $\zeta |P_{\sigma}(\mathbf{r},t)|^2$; ζ is the dimensional reservoir response constant⁴⁸; R describes the stimulated scattering rate from the reservoir to the ground state; and γ and γ_0 are the decay rates of polaritons and reservoir excitons, respectively.

We used values of the parameters estimated from the experiment for the simulation. We used decay rates $\gamma=1/200\,{\rm fs^{-1}}$ and $\gamma_{\rm R}=1/390\,{\rm fs^{-1}}$. The pump energy is resonant to the polariton energy at $k=1.5\,{\rm \mu m^{-1}}$. The L–T splitting is taken as $\Delta k^2=0.75\,{\rm meV}$ (at the same k), which is typical for such structures. To estimate the interaction constants, we refer to the analyses performed in refs. 49,50 . The exciton–exciton interaction constant is approximated as $\alpha_{\rm R}\approx cE_{\rm b}a_{\rm B}^2$, where $E_{\rm b}$ and $a_{\rm B}$ are the exciton binding energy and the Bohr radius, respectively, and c is the numerical constant. For the characteristic parameters $E_{\rm b}=0.5\,{\rm eV}$, $a_{\rm B}=2\,{\rm nm}$ and c=2, the interaction constants are estimated as $\alpha/X^2=\alpha_{\rm R}=4\,{\rm \mu eV}\,{\rm \mu m^2}$. For R, the following approximation from the Fermi golden rule holds: $R\propto E_{\rm b}a_{\rm B}^2/\hbar$, which gives $R\approx 0.005\,{\rm ps^{-1}\,\mu m^2}$.

Data availability

The data that support the findings of this study are available from the corresponding author on reasonable request.

References

- Schmidt., D. et al. Tracking dark excitons with exciton polaritons in semiconductor microcavities. Phys. Rev. Lett. 122, 047403 (2019).
- Tassone, F. & Yamamoto, Y. Exciton-exciton scattering dynamics in a semiconductor microcavity and stimulated scattering into polaritons. *Phys. Rev. B* 59, 10830 (1999).
- Shahnazaryan, V., Iorsh, I., Shelykh, I. A. & Kyriienko, O. Exciton-exciton interaction in transition-metal dichalcogenide monolayers. *Phys. Rev. B* 96, 115409 (2017).